NEUROSCIENCE

Modular architecture facilitates noise-driven control of synchrony in neuronal networks

Hideaki Yamamoto[1,2]*†, F. Paul Spitzner[3]†, Taiki Takemuro[1,4], Victor Buendía[5,6,7], Hakuba Murota[1,2], Carla Morante[8,9], Tomohiro Konno[10], Shigeo Sato[1,2], Ayumi Hirano-Iwata[1,2,4,11], Anna Levina[5,6], Viola Priesemann[3,12]‡, Miguel A. Muñoz[7,13]‡, Johannes Zierenberg[3]‡, Jordi Soriano[8,9]‡*

High-level information processing in the mammalian cortex requires both segregated processing in specialized circuits and integration across multiple circuits. One possible way to implement these seemingly opposing demands is by flexibly switching between states with different levels of synchrony. However, the mechanisms behind the control of complex synchronization patterns in neuronal networks remain elusive. Here, we use precision neuroengineering to manipulate and stimulate networks of cortical neurons in vitro, in combination with an in silico model of spiking neurons and a mesoscopic model of stochastically coupled modules to show that (i) a modular architecture enhances the sensitivity of the network to noise delivered as external asynchronous stimulation and that (ii) the persistent depletion of synaptic resources in stimulated neurons is the underlying mechanism for this effect. Together, our results demonstrate that the inherent dynamical state in structured networks of excitable units is determined by both its modular architecture and the properties of the external inputs.

INTRODUCTION

The mammalian brain is in a state of perpetual ongoing activity characterized by high levels of irregularity in single-neuron response [1, 2] and correlated fluctuations across brain regions [3–7]. Understanding the origin and functional significance of such neuronal activity has been challenging for both physics and neuroscience, and diverse competing hypotheses have been proposed to rationalize its nature. A compelling concept in statistical physics is that cortical networks operate nearby a critical point, i.e., at the edge of a nonequilibrium phase transition [8–15]. One possibility is that such a transition separates synchronous and asynchronous phases [16, 17]. Synchrony in this context refers to the collective activation of neurons in a fast-cascading event, a phenomenon also referred to as neuronal avalanches [8, 18]. Such synchronous states can be argued to enable coherent or robust information transfer integrated across distance and time [19], while asynchronous states have been argued to enable segregated processing in local circuits with reduced redundancy [17]. Flexible switching between states with different levels of synchrony would enable networks to transiently exploit diverse functional advantages, all the most in modular networks where the phase transition can be very broad, with a rich hierarchy of intermediate states of partial synchronization [20].

Transitions between synchronized and desynchronized states are well-known to occur in the mammalian brain and have mostly been described in the context of dynamical properties of individual neurons [21] and the dynamical consequences of the network architectures they form [20–27]. Recent findings, however, suggest that such transitions can also be induced depending on the nature of external inputs [28, 29]. For instance, the thalamus projects asynchronous background inputs to the cortex [30–32], which decreases the level of synchrony. Consistent with this, anesthesia, which reduces the thalamocortical input [33], enhances neuronal synchrony in the rat somatosensory cortex [34]. The deprivation of such inputs by anatomical lesions has also been shown to increase cortical synchrony and generate epileptic seizure-like activity in slice preparations [35]. Meanwhile, theoretical studies reveal that the response of a generic network to external perturbations strongly depends on network architecture and on the strength of synaptic interactions [36]. Therefore, given that cortical networks are nonrandom [37] and exhibit strong modularity [5, 38–43], it is reasonable to hypothesize that cortical dynamics rely on the underlying network architecture in conjunction with the asynchronous input they constantly receive from subcortical areas, such as the thalamus. However, despite the accumulated evidence, the actual mechanisms that allow cortical networks to transiently regulate their level of synchronization remains elusive, both experimentally and theoretically.

To fill this gap, here, we use in vitro cortical networks grown on engineered substrates [44]. Three different types of modular networks with diverse degrees of modularity were grown, and their responses to asynchronous stimulation delivered via optogenetics were assessed using fluorescence calcium imaging. The results show that modularity, together with asynchronous external input, enhances the dynamical repertoire by fostering desynchronization. This effect weakens when inhibitory synapses are pharmacologically

[1]Research Institute of Electrical Communication (RIEC), Tohoku University, Sendai, Japan. [2]Graduate School of Engineering, Tohoku University, Sendai, Japan. [3]Max Planck Institute for Dynamics and Self-Organization, Göttingen, Germany. [4]Graduate School of Biomedical Engineering, Tohoku University, Sendai, Japan. [5]Max Planck Institute for Biological Cybernetics, Tübingen, Germany. [6]Department of Computer Science, University of Tübingen, Tübingen, Germany. [7]Departamento de Electromagnetismo y Física de la Materia, Universidad de Granada, Granada, Spain. [8]Departament de Física de la Matèria Condensada, Universitat de Barcelona, Barcelona, Spain. [9]Universitat de Barcelona Institute of Complex Systems (UBICS), Barcelona, Spain. [10]Graduate School of Pharmaceutical Sciences, Tohoku University, Sendai, Japan. [11]Advanced Institute for Materials Research (WPI-AIMR), Tohoku University, Sendai, Japan. [12]Institute for the Dynamics of Complex Systems, University of Göttingen, Göttingen, Germany. [13]Instituto Carlos I de Física Teórica y Computacional, Universidad de Granada, Granada, Spain.
*Corresponding author. Email: hideaki.yamamoto.e3@tohoku.ac.jp (H.Y.); jordi.soriano@ub.edu (J.S.)
†These authors contributed equally to this work.
‡These authors contributed equally to this work.

blocked, i.e., when the network is purely excitatory driven. The results are then compared with in silico analyses of a spiking neural network model to show that a combination of sparser (stochastic) intermodular interactions and decreased level of available synaptic resources is the underlying mechanism behind the experimentally observed desynchronization. Last, we derive a mesoscopic model incorporating a state-dependent gating of intermodular interactions that allows us to rationalize the previous results in a parsimonious way. Together, our findings demonstrate a potential network mechanism by which asynchronous input can serve as a control parameter for tuning the dynamical state of structured neuronal networks.

RESULTS

Disruption of synchrony by optogenetic stimulation

We first assessed how external perturbations influence synchronized neuronal activity in networks of primary cortical neurons, containing both excitatory and inhibitory neurons, grown in vitro. We designed ring-modular micropatterns consisting of four small squares (200 μm by 200 μm each) with connection lines that allowed a fraction of the neurites to interconnect the squares (Fig. 1A). The neuronal activity of the micropatterned networks was recorded by fluorescence calcium imaging using the calcium probe GCaMP6s (Fig. 1B and movies S1 and S2), which was virally expressed under the Synapsin promoter that transduces both excitatory and inhibitory neuronal populations in the cortex (45). Neurons were perturbed either by irradiating patterned light to individual neurons transfected with the photoactivatable cation channel ChrimsonR (optogenetic stimulation; Fig. 1C) expressed in both excitatory and inhibitory populations or by increasing the extracellular potassium concentration $[K^+]_o$ (chemical stimulation). The former induces spiking activity in targeted neurons (46), whereas the latter increases the frequency of collective activity of neurons in the entire culture, effectively raising the overall neuronal excitability (47).

In the nonstimulated state (Fig. 1D), the activity of the cultures was characterized by quasi-periodic episodes of network-wide bursting activity with some variability in population rate amplitude due to the modular architecture (44). External perturbation via optogenetic stimulation induced a qualitative change in network dynamics. This stimulation was delivered as alternating patterns of red light illuminating the soma of up to 10 neurons selected from the lower two of the four modules (Fig. 1A). Only the neurons expressing ChrimsonR were selected as potential targets, with no imposed bias in excitatory/inhibitory cell types. The illumination pattern was switched every 400 ms, and in each time window, each neuron was targeted with a probability of 40%. During stimulation, the frequency of collective events as well as the variety of activity patterns increased (Fig. 1, E and G). These enriched network dynamics were observed during ongoing stimulation and diminished when it was switched off (Fig. 1F). Representative snapshots of network behavior before, during, and after stimulation are provided in Fig. 1G, illustrating the shift in collective activity from a synchronized to a desynchronized state upon optogenetic (asynchronous) stimulation. Such a transient shift in the network state was also observed when the asynchronous stimulation was delivered to all four modules and when a uniform stimulation was delivered locally to one of the modules (see section S1B and fig. S1 for details). In

contrast, chemical stimulation imposed a qualitatively different change in network dynamics (Fig. 1, H and I, and movies S3 and S4). Contrary to optogenetic stimulation, network-wide collective activity remained dominant, even in the perturbed state. These results indicate that a mere increase in excitability was insufficient and that an asynchronous stimulation was necessary to break synchrony and increase the dynamical repertoire of the cortical cultures.

Changes in collective activity during stimulation were quantified by measuring the distribution of event sizes, i.e., the fraction of neurons entrained in each collective activity episode (Fig. 1J, left). Optogenetic stimulation led to a significant decrease in event size indicating a loss of synchrony. This change was accompanied by a decreased median and a broadened distribution of pairwise correlation coefficients (Fig. 1J, middle), the latter of which manifested in an increased functional complexity (Fig. 1J, right), a signature of enhanced integration-segregation balance (48). Chemical stimulation, however, preserved synchrony in network dynamics and showed the opposite trend in both the event size and functional complexity.

The overall effect induced by optogenetic stimulation was abolished in the presence of bicuculline (20 μM), a γ-aminobutyric acid type A receptor antagonist that blocks inhibitory synapses, and the effect was thus γ-aminobutyric acid (GABA) dependent (fig. S2 and movies S5 and S6). This indicates that GABAergic balancing of excitation and inhibition (49, 50) is required for external input to alter the network dynamics. This observation suggests that when a network is in an exceedingly excited state, neurons become mostly depleted of neurotransmitters between collective activity events (51, 52), leading to a state that is insensitive to perturbations.

Impact of modular architecture

Next, we assessed how the effect of asynchronous stimulation depends on the network topology, specifically its modular architecture. Hence, we prepared three types of networks with a constant number of neurons and different degrees of modularity (Fig. 2, top drawings, and fig. S3). The modular micropattern used in the aforementioned experiments is hereafter referred to as the "single-bond" (1-b) micropattern. Similarly, a "triple-bond" (3-b) micropattern was designed by increasing the number of connection lines to three. Last, the "merged" micropattern was a single square of 400 μm by 400 μm. The modularity of the network, defined as the fraction of intramodular connections within a network greater than the expected fraction in a random network, decreased in the order of 1-b, 3-b, and merged (44, 53).

A comparison of the distribution of event sizes and correlation coefficients between these three cases revealed that noise perturbations have stronger effects when modularity is higher. As shown in Fig. 2A, the decrease in median event size via optogenetic stimulation was 54% for the 1-b network, whereas the values were 21 and 25% for the 3-b and merged networks, respectively. A similar trend in structure dependence was also observed for the correlation coefficients (Fig. 2B), which decreased by 49, 13, and 19% for the 1-b, 3-b, and merged networks, respectively. To understand the mechanism of this structure dependence, we analyzed the shift in the correlation coefficient between two generic neurons i-j, r_{ij}, during perturbation (Fig. 2C). For the 1-b network, the decrease in correlation largely stemmed from the neuron pairs that included at least one stimulated neuron, in which case r_{ij} broadly scattered below the
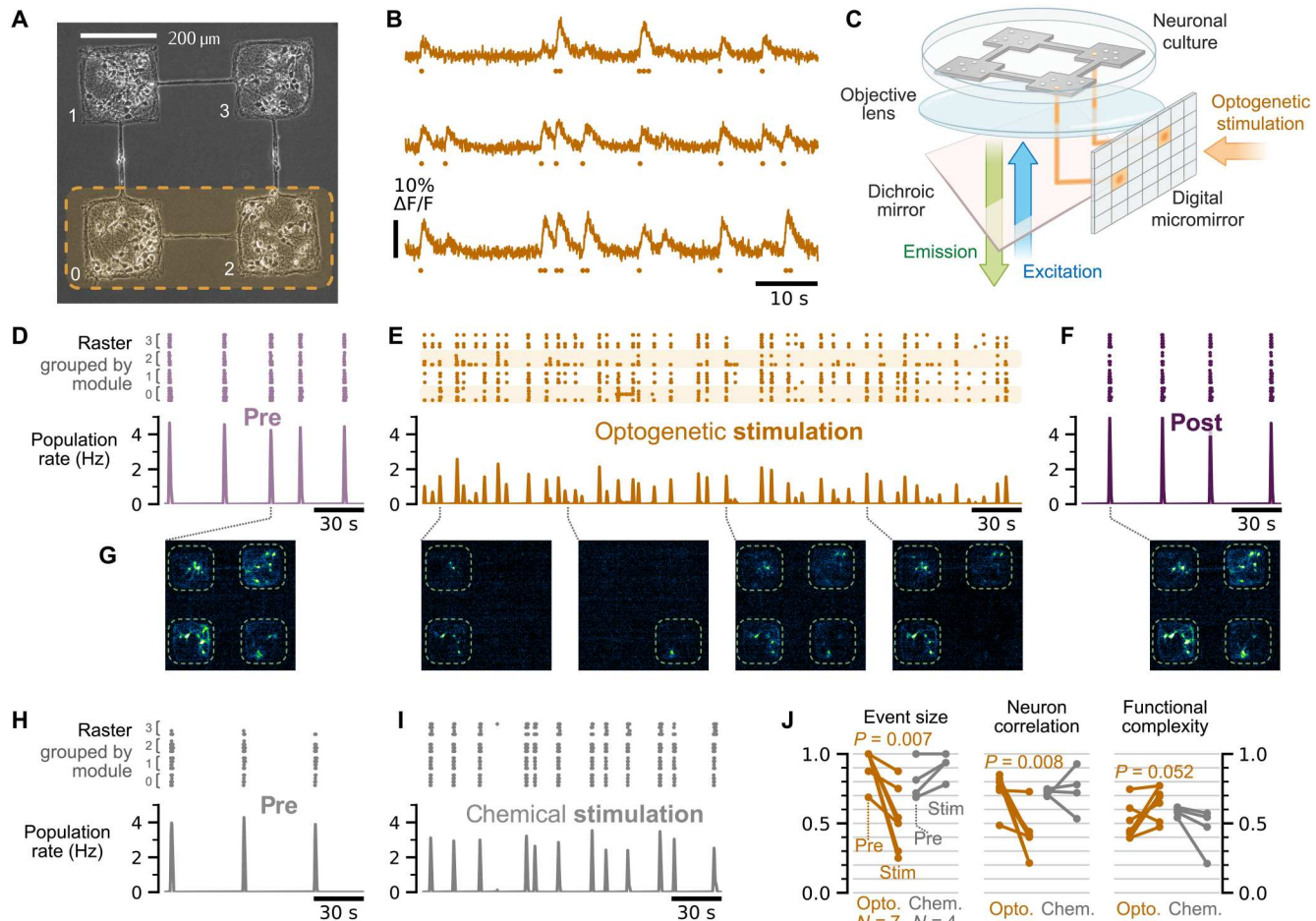
Fig. 1. Optogenetic stimulation on modular neuronal cultures increases the variability in collective network dynamics. (**A**) Phase-contrast image of a representative single-bond modular network. Neurons appear as dark round objects with a white contour. Ten neurons were selected from the bottom module pair (orange box) and optogenetically targeted in a random manner. (**B**) Representative fluorescence traces and inferred spike events (dots) of three neurons along 1 min. (**C**) Sketch of the experimental setup. Neuronal cultures were transfected with ChrimsonR for optogenetic stimulation (orange arrow) and GCaMP6s for simultaneous activity monitoring (blue and green arrows). (**D**) Pre-stimulation raster plot (top panel) of network spontaneous activity, with neurons grouped according to their module, and the corresponding population activity (bottom). (**E**) Corresponding data upon optogenetic stimulation, wherein population activity markedly increases in variability. Targeted modules are marked as orange bands. (**F**) Spontaneous activity post-stimulation, with a return to strong network-wide bursting. (**G**) Representative snapshots of calcium imaging recordings for the above data. All modules activate synchronously without stimulation. Upon stimulation, activity events extend over individual neurons, multiple modules, or all modules. (**H** and **I**) Raster plot and population activity before and during chemical stimulation. Chemical stimulation increases the frequency of events but maintains the network-wide activity. (**J**) Effect of optogenetic and chemical stimulation on bursting median event sizes, median correlation coefficients, and functional complexity (paired-sample t test, two-sided). For chemical stimulation with $N = 4$, no test was performed.

unit line in the pre-stim plane. The median r_{ij} strongly decreased when either one or both neurons in a pair were located within the stimulated modules, a feature that was not observed for neuron pairs in unstimulated modules (Fig. 2D). The spatial dependence was less pronounced when modularity was low (3-b) or absent (merged).

The tendency for strongly modular networks (1-b pattern) to be more sensitive to the optogenetic perturbation was also evident in the realization-level estimates (Fig. 2, E to H). These changes were independent of firing rate (Fig. 2E). In addition, the broadened distribution of correlation coefficients during stimulation increased the value of functional complexity (Fig. 2H), which was largest in the 1-b network under stimulation. Summarizing, modularity fostered local and transient decorrelation from asynchronous

stimulation to dampen the collective activity events that propagate globally throughout the entire network.

Microscopic spiking neural network model

To rationalize the underlying mechanisms behind the enhanced sensitivity to external perturbations in modular networks, we next constructed a spiking neural network (SNN) model based on leaky integrate-and-fire (LIF) neurons (see Materials and Methods, section S2, and movies S7 and S8 for details). The networks were generated on the basis of the metric construction approach described previously (*18*), and modularity was tuned by specifying the number of axons k that crossed from one module to another (Fig. 3, A and B). To control the modularity while retaining the overall connectivity, the mean in-degree of neurons was fixed to
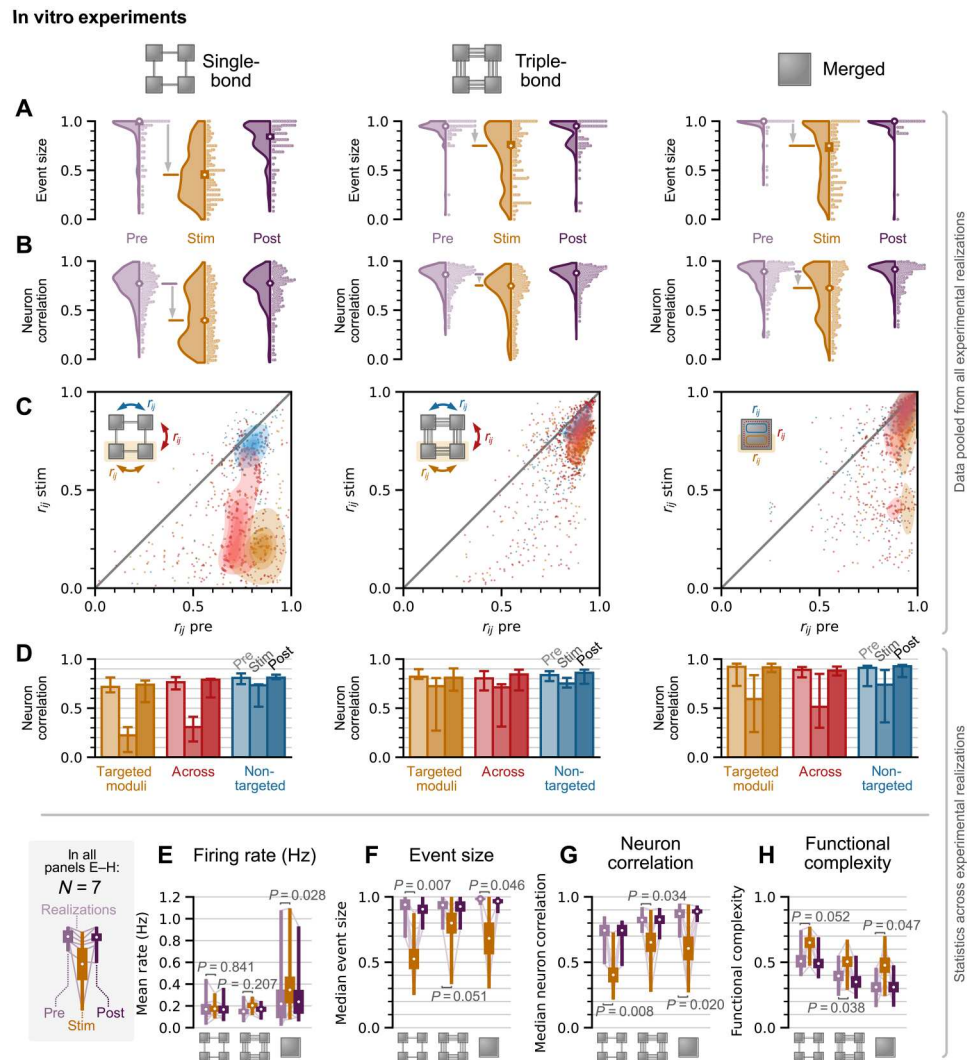
In vitro experiments

Fig. 2. Disruption of network-wide collective activity upon optogenetic stimulation is facilitated by modular architecture. (**A**) From left to right, event size distribution before, during, and after optogenetic stimulation for the 1-b, 3-b, and merged networks. Violin plots (left side of distribution) represent smooth kernel estimates of the events observed across all networks, while individual observations are shown in swarms (right side). Error bars (middle) are obtained via bootstrapping. White dots indicate the median of the 500 bootstrap estimates, and bars represent the 95 percentiles. (**B**) Corresponding distribution of pairwise Pearson correlation coefficients between neurons calculated from binned spike counts. A substantial drop is only observed for 1-b. Data are presented as in (A). (**C**) Change of correlation coefficients r_{ij} between the pre-stimulated and stimulated conditions, grouped according to the regions in which neurons are located. Both neurons may either reside in regions that are targeted by stimulation (yellow), both reside in nontargeted regions (blue), or the pair spans across a targeted and nontargeted regions (red). For modular networks, the regions correspond directly to modules. Decorrelation is more pronounced when one or both neurons are in regions that are targeted. Colored areas are fitted probability density estimates for each data group. (**D**) Same as (C) but showing realization-level statistics. Bar heights represent the medians of independent estimates in each realization, and error bars represent 95 percentiles. cf. table S7. (**E** to **H**) Estimates for each realization: mean firing rates (E), median event sizes (F), median correlation coefficients (G), and functional complexity (H) for the three topologies. Thin lines, individual realizations (networks); white dots, means of 500 bootstrap samples; thick bars, SEM; thin bars, extrema. *P* values are from paired-sample *t* test (two-sided), cf. tables S1 and S7.

be the same in all topologies (fig. S4). Spontaneous activity was driven by Poisson noise, representing the spontaneous release of neurotransmitters in biological presynaptic terminals (*18, 51*). Note that we focus on the optogenetic stimulation, as the change in the extracellular potassium concentration induced in the chemical stimulation does not simply translate to a single parameter in the LIF model. With $k = 3$, we obtained dynamic behaviors comparable to experiments in 1-b networks (Fig. 3, C and D). The model accurately recapitulated the experimental observations made in the

optogenetic stimulation paradigm. In the pre-stimulated state (Fig. 3C), activity patterns composed of sporadic activity with reoccurring network-wide events. Stimulation, introduced in the two lower modules as an additional noise input (mimicking inward current pulses from optogenetic inputs), led to a breakdown of synchrony among modules and an increase of events localized to a fraction of modules (Fig. 3D). As shown in the panels of Fig. 3E, the median event size decreased from 0.81 to 0.27, and the median correlation among neuron pairs decreased from 0.84 to 0.58 (cf. table
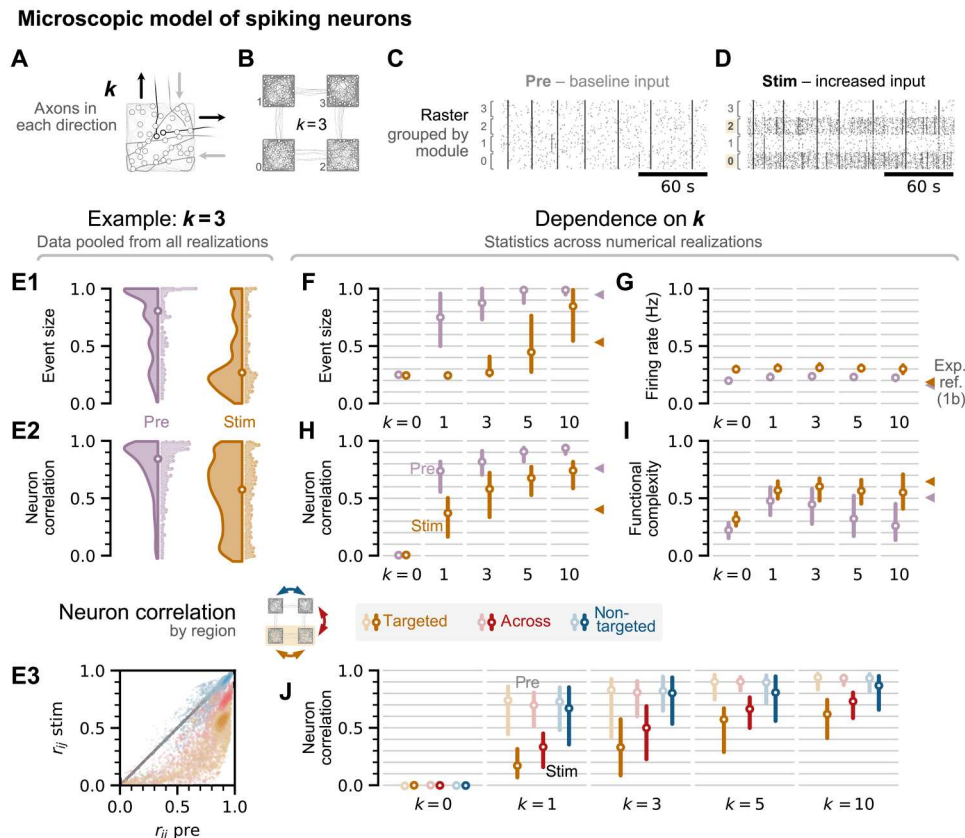
Fig. 3. Microscopic-level simulations of modular networks using LIF neuron models. (**A**) Sketch of a single module, where k axons connect to each adjacent neighbor (shown for $k = 1$). (**B**) Sketch of a simulated modular network with $k = 3$. (**C** and **D**) Representative raster plots in the pre-stimulated (C) and stimulated (D) regimes. Modules targeted with an increased noise are #0 and #2. (**E1** and **E2**) Joint distributions of event size and pairwise correlation coefficients from data pooled from 50 independent numerical realizations, comparing pre and stim conditions. Both distributions exhibit a substantial drop towards smaller values upon stimulation. White dots are the median of 500 bootstrap estimates, and error bars representing the 95 percentiles are smaller than the symbol size. (**E3**) Change of correlation coefficients r_{ij} between the pre-stimulated and stimulated conditions (yellow: neuronal pairs reside in target modules; blue: reside in nontargeted; red: span across a target and a nontargeted module). The diagonal black line is the no-change reference condition. As in the experiments, decorrelation is more pronounced when one or both neurons are in modules with increased noise. (**F** to **I**) Dependence of four descriptors (event size, firing rate, neuron correlation, and functional complexity) on k. The higher k, the lower the modularity of the networks. Statistics are obtained across realizations where each realization yields a single scalar. White dots are the median of single-realization estimates. Rounded bars are 68 percentiles, indicating the variability between realizations. Triangles on the right of each panel indicate the values from single-bond experiments. (**J**) Correlation of neuron pairs grouped by the neurons' respective modules (yellow, red, and blue). For each k, the pre- and post-conditions are compared (faint versus dark colors). The strongest decorrelation is observed when both neurons are in noise-targeted modules (yellow) or modularity is high ($k = 1$ and 3).

S6). Corroborating the experiments, a greater decrease in the correlation coefficient was observed for cell pairs wherein one of the cells belonged to the targeted modules (Fig. 3, E and J), whereas the change was less pronounced for cell pairs in nontargeted modules.

For a systematic investigation of the effect of network modularity, we explored topologies with different numbers of axons crossing the modules: $k = 1, 3, 5,$ and 10, corresponding to modularity $Q = 0.71, 0.62, 0.53,$ and $0.32,$ respectively (cf. section S2B for analytical details). The simulations showed that desynchronization caused by stimulation strongly depends on the underlying network topology (Fig. 3, F to I). As a general trend, the event sizes and pairwise correlations increased with k due to increased coupling between modules (44). In the absence of any intermodular connection ($k = 0$) event sizes and correlation coefficients correspond to activity that is confined to individual modules (synchronized only at chance level) and, as expected, stimulation had little effect.

For $k > 0$, the presence of additional noise input (stim) decreased the median event size (Fig. 3F), and at low coupling ($k = 1$ and 3), event sizes consistently reached the single-module level. For higher coupling ($k = 5$ and 10) and in the absence of stimulation, the system was synchronous (with event sizes ~1), and stimulation caused a decrease to intermediate values. Note that the percentile bars (Fig. 3, F to J) represent the variability between realizations, which stems from the randomness in the amount of actual connections that are formed by bridging axons. This stresses that the response to noise stimulation, and thus the sensitivity of the network, is strongly constrained by its topology.

Pairwise correlations (Fig. 3H) showed a similar trend, where networks with low k were already quite desynchronized even without stimulation. Networks with larger k also desynchronized upon stimulation, but median values did not go as low as those for low k. Since the functional complexity (Fig. 3I) is maximal for

a flat distribution of correlation coefficients (*48*), large values coincide with a median correlation near 0.5. Consistently, the functional complexity is maximal for $k = 1$ and 3. Correlation distributions at those k are already broad without stimulation (Fig. 3E2), and therefore, the effect of stimulation on functional complexity is stronger at higher k. We note that, for all k, these observations were independent of the changes in firing rates, which were consistent across networks (Fig. 3G, see also fig. S7).

Overall, simulations confirmed that the coupling between modules shapes the impact of the noise input, with the effect most prominently visible in the regions that directly received stimulation (Fig. 3J). The coupling between modules—which, besides from k, depends on the particular network realization—forms the substrate for dynamics that are then mediated by the noise level. For instance, highly modular networks ($k = 1$ and 3) feature rich dynamics already at baseline (pre, Fig. 3, F and I), but less modular networks ($k = 5$) may still be enriched through noisy input (stim, Fig. 3, F and I). However, strong coupling between modules ($k = 10$) may lock the system in an integrated state where the additional noise only mildly decreases the median event size and neuron correlations. This can be explained by the heterogeneous degree distributions (cf. fig. S5): The connectivity between modules scales with k and affects the probability of activity spreading between modules (fig. S6), while the connectivity within modules is always high, so that modules are effectively synchronized units.

Network mechanisms: The importance of synaptic resources

To understand the network mechanisms that enable the increased sensitivity to external noise input in modular networks, we analyzed the dynamics of synaptic resources in each simulated neuron. For this purpose, we plotted the evolution of the mean synaptic resources in each module as a function of the module-averaged firing rate of the neurons. The characteristic behaviors of the mean synaptic resources $R \in [0, 1]$ are depicted in Fig. 4 (A to C). Abrupt discharges during bursting events are followed by gradual recharges between the events. In the baseline condition (pre), R had a maximal value of ~0.8 when charged but dropped to ~0.3 after network-wide bursting events. When neurons were subjected to additional noise input (stim), R of the targeted modules (Fig. 4B, orange trajectories) only recovered to ~0.5, effectively reducing the synaptic efficacy. While, in general, R of the nontargeted modules (blue trajectories) was only indirectly affected by the stimulation, the precise cycles depended on the individual realizations (cf. dark blue versus light blue, Fig. 4, B and C). Independent of the network architecture, increased noise decreased the overall size of the cycles in targeted modules, but modularity still affected cycles of nontargeted modules (fig. S4). This stresses that the combination of network topology and asynchronous stimulation determines the charge-discharge dynamics on the module level.

To complete these results, we investigated how the degree of synchrony between modules changed with the strength of external input, as parameterized here by its frequency (Fig. 4D). In general, we observed that the correlation between module-level firing rates of targeted modules (Fig. 4D, top) decreased with stimulation but that stronger noise was required for larger k. For example, in $k = 1$ networks, an increase of 10 Hz in external input reduced correlation from 0.4 to 0.25, but to cause the same drop in correlation for $k = 10$, an increase of about 25 Hz was

required. To further illustrate the effect of noise on modular networks, we revisited $k = 3$ and computed the fraction of events that spanned a given number of modules, from 1 to 4 (Fig. 4D, bottom; cf. zoom-ins in Fig. 4C). Without stimulation, about 50% of the events encompassed the four modules, i.e., network-wide bursting. The addition of noise of just 10 Hz provided a more balanced dynamics in which the occurrence of 1-module and 4-module activations was both about 35%.

Mesoscopic description

As illustrated in the raster plots for both the pre and stim cases (Fig. 4C, insets), in which neurons activate in a quasi-synchronous manner within each module, much of the noise-induced changes in network dynamics occurred between modules. This implies that, to study global effects, some microscopic details can be neglected and that modules can be reduced to an effective dynamical unit. Thus, to extrapolate the microscopic behavior of individual neurons to the macroscopic dynamics, we built a mesoscopic module-level model that captures the key empirical results. Here, the dynamics of each module were described by a rate model with resource depletion (*12*), where two coupled differential equations represent the evolution of firing rate ρ and synaptic resources R, respectively (see Materials and Methods and section S3A for details).

As a first exploration of the model, we considered the case in which each module received input through a nonlinear activation function that depended on the rate and resources of the connected modules and an external input that captured the main (average) effect of stimulation. In such a case, increasing the amplitude of external input (which reflects enhanced stimulation frequency in both the experiments and the microscopic model) decreased the size of the resource-rate cycles of each module but did not affect synchronization (fig. S10). Thus, we introduced nondeterministic intermodular interactions as "gates" that stochastically disconnect when synaptic resources are depleted and reconnect after a characteristic time (Fig. 4E and section S3C). The stochastic gating reflects the following neuron-level dynamics which we embedded into the underlying module-level equations (figs. S11 and S12): When a module starts bursting, resources of all involved neurons are rapidly consumed, so that also those connecting to other modules will not transmit activity. Accordingly, outgoing gates will deactivate with a short time constant and remain disconnected for a relatively long time while neuron resources recharge. In this period, should the module bursts again, the propagation of activity to other modules hinges on the few intermodular connections and is less probable to spread. This probability is reflected by the gate being already reconnected or not. If still disconnected, activity cannot spread to the neighboring modules. Hence, if modules tend to burst with a time scale faster than the gate recovery, the mutual entrainment of activity between modules is hindered, because the crucial initiating inputs cannot pass through the disconnected gates, and, therefore, the system cannot synchronize. Thus, these gates capture the essence of the microscopic dynamics—wherein intermodular coupling only operates when the synapses projecting from one module to another are not fully depleted—on the mesoscopic level.

Numerical simulations revealed that the addition of the gating mechanism was indeed sufficient to recapitulate the noise-dependent breakdown of synchrony observed in the experiments and SNN model (Fig. 4, B and C versus Fig. 4, F and G). Network-
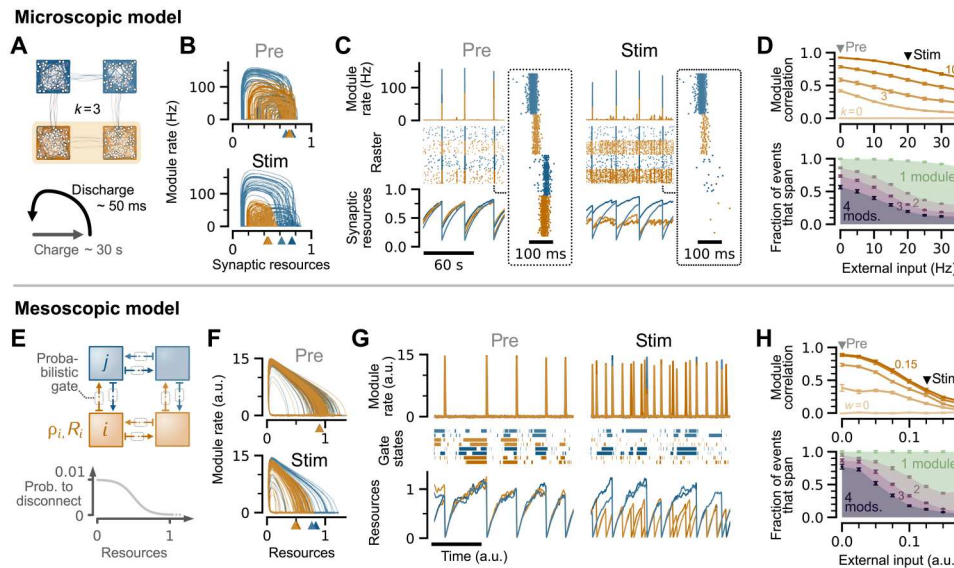
Fig. 4. Desynchronization can be understood through charge-discharge cycles in the resource-rate plane, which is captured by a minimal mesoscopic model. (Top row) Microscopic model using LIF neurons. (Bottom row) Mesoscopic model, where modules are the smallest functional unit. (**A**) Top: Sketch of the microscopic model, in which orange modules are those targeted by an increased noise. Bottom: Conceptual representation of the resource-rate cycles and the contrasting timescales involved. (**B**) Resource-rate cycles in a representative simulation with $k = 3$. Orange trajectories correspond to targeted modules, and blue trajectories correspond to nontargeted ones. Under stimulation, resources are more depleted on average (smaller excursions), and discharge events start at lower resources (colored triangles). (**C**) Module-level firing rates, raster plot, and average module-level resources under pre and stim conditions. Insets show a detail of neuronal activity during a network-wide activity event. (**D**) Top: Correlation between module-level firing rates of targeted modules as a function of the external input (added noise). Curves from bottom to top correspond to gradually higher k values. Triangles indicate the the values of external input for the pre and stim conditions, from which the cycles and raster plots of (B) and (C) are built. Bottom: Average fraction of modules that participate in an event for $k = 3$ as a function of external input. (**E**) Top: Sketch of the mesoscopic model with probabilistic gates between modules. Bottom: Gates have a high probability to disconnect when resources of the source module are low. (**F**) Resource-rate cycles and the effect of stimulation for the mesoscopic model. (**G**) Module rate, gate state (solid when connected), and module resources as a function of time. Note the disconnection of gates after high-rate discharge events. (**H**) Top: Correlation of the firing rates of targeted modules as a function of the external input. Bottom: Average fraction of modules involved in events ($w = 0.1$). a.u., arbitrary units.

wide events were decreased under stimulation (Fig. 4, G and H), despite stimulated modules remaining in a more oscillatory regime than in the SNN (stim condition in Fig. 4G). Yet, the mesoscopic model successfully captured the noise-dependent reduction of intermodular correlation with external input and its dependence on the coupling strength (here denoted by w; Fig. 4H, top). Weakly coupled networks (low w) exhibited a systematic lower correlation than strongly coupled ones (high w). Similarly to the SNN model, the fraction of events that spanned a given number of modules for medium $w = 0.1$ quickly changed from a 4-module dominated regime in the absence of stimulation to a richer repertoire of activation patterns for increased external input (Fig. 4H, bottom).

Furthermore, the simplicity of the mesoscopic model allows for an analytic understanding of the input-dependent change in the size of resource-rate cycles (fig. S10). In the resource-rate plane, the fixed point corresponding to a charging, nonfiring module i that receives no input is at $(\rho_i, R_i) = (0,1)$. Spontaneous fluctuations (depending on external input and noise) may push the module out of its (slow, $\rho = 0$) path toward the fixed point and ignite a burst along the flow field in the resource-rate plane (fig. S10). As the external input to a module effectively reduces the activation threshold, it determines how easily a burst can be ignited. During a burst, the trajectory moves fast at high rates in the negative R direction, due to the small-time constants of the rate equation (τ_ρ) and of the discharge term (τ_d). However, the trajectory is slow in the positive R direction

due to the large time constant in the resource charge term (τ_c). Thus, at large external inputs (low threshold), a module may start a burst before completing its slow return to the fixed point, which explains the reduced cycle size. Further details and the mechanisms linking resource cycles to the synchronization between modules are provided in section S3B. In summary, the simple mesoscopic approach elucidates the critical role of stochastic intermodular interaction in determining the network dynamics of modular networks and provides an intuitive understanding of the noise-induced breakdown of synchrony in modular neuronal networks.

DISCUSSION

Taking advantage of in vitro experiments using cultured neuronal networks as a model biological system, we showed that modular architecture enhances the sensitivity of the network to external asynchronous perturbation. In particular, network-wide collective bursts are much reduced in the presence of modular structures driven by noise. This occurs only when noise is asynchronous (optogenetic stimulation of targeted neurons) and not homogeneous across the network (chemical stimulation) and happens only in balanced networks, while when inhibition is blocked, bursty events persist even in the presence of noise. Furthermore, computational in silico modeling enabled us to identify the mechanisms behind the noise-driven decrease of synchrony reported in experiments.

Focusing on the modular architecture that entrains burst-like activity within modules and stochastically propagated activity across modules (*44*, *54*, *55*), we showed that asynchronous input reduces the average level of synaptic resources, which only weakly affects activity propagation within modules but decreases the probability to propagate activity across modules. This can be understood at the neuron level, where the probability of a neuron to spike depends on the strength and number of incoming synaptic connections. Whereas the reduction of average synaptic resources affects the synaptic strengths in all neurons, the modular architecture only reduces the expected number of connections between neurons of different modules, which together results in the reduction of activity propagation across modules (fig. S6). Hence, our results extend previous theoretical studies that identified the strength of external noise as control parameter to interpolate between bursting and reverberating dynamics in neural networks (*29*).

To demonstrate the robustness of our results, we coarse-grained our microscopic simulations of spiking neurons into a mesoscopic model (*12*), where the depletion of resources is expressed in a minimalistic way. In both micro and meso approaches, stochastic intermodular connections were essential and were grounded on the heterogeneous degree distribution in the spiking neuron model and the gating mechanism in the mesoscopic one.

Our mesoscopic description opens an intriguing perspective: As we have shown, a coarse description of neuron populations through scalar variables can suffice to capture those dynamics that are most relevant on large scales, which was also explored recently in hippocampal networks (*56*). This is implicitly often assumed, for instance, whenever measures such as local-field potentials are used. In such cases, single-neuron dynamics cannot be inferred, raising valid criticism about the gained understanding of population dynamics (*57*). Our comparison between microscopic and mesoscopic dynamics supports that—if the applied coarse scale is correct—such population-level measures are indeed sufficient to study the large-scale dynamics. As a related remark, we note that an ensemble of quadratic LIF neurons, such as those used in here as the spiking neuron model, could, in principle, be represented in the mean field (*58*–*60*), even with limited stochastic noise (*61*). While not applicable for our small and noise-driven modules, the mean-field approach can provide a complementary theoretical description in cases where the assumption of near infinite size and low noise are justified.

In a more general scope, noise is a ubiquitous property of brain networks. For example, while the fundamental role of the thalamus is to relay peripheral sensory information to the cortex (*62*), thalamic neurons are also known to deliver asynchronous, weakly correlated inputs to the cortex in the spontaneous state (*30*). Intracellular recordings in the barrel cortex also show that the temporal correlation of membrane potential fluctuations is close to zero when the cortex is driven solely by the thalamus (*31*). Such input from subcortical areas could act merely as a source of noise, but it could also change the dynamical state of the targeted cortical region to modulate its stimulus sensitivity, dynamical repertoires, and computational capabilities (*9*, *13*, *14*, *63*). By adapting a ubiquitous property of brain networks (in vivo) to well-controlled cultures of cortical neurons (in vitro), our work provides an understanding of how asynchronous inputs modulate the ongoing activity of cortical networks.

In previous studies, electrical stimulation with multielectrode arrays (*64*–*66*) and more recently optogenetic stimulation (*67*) have been used to show that multisite stimulation effectively reduces the occurrence of collective activity events in cortical cultures on uniform substrates. These experimental investigations correspond to the merged topology of our study, wherein a similar suppression of collective events has been confirmed, even if at a smaller degree than in highly modular preparations. A number of works (*64*, *66*, *67*) also suggested a plastic change induced in network dynamics, an effect that was not observed in the present study. The difference could originate not only from the culture age or the duration of stimulation but also from extracellular calcium condition (*68*), opening future applications of in vitro cortical networks to the understanding of the cellular mechanisms underlying learning and memory. Besides the precision micropatterning approach used in the present work, the overall extent of network modularity can also be controlled through the modulation of cell affinity of the scaffold (*54*, *55*) or through pharmacological manipulation of neurite outgrowth (*69*, *70*), which could be beneficial in tuning network structures at a larger scale.

We note that twenty percent of neurons in the mammalian cortex are inhibitory, with some variation across species and areas (*71*, *72*), and this presence of inhibition is believed to be crucial for computational purposes (*17*). Our experiments revealed that GABAergic inhibition is necessary for the neuronal network to modulate its level of synchrony, because when inhibition was blocked, synchronous epileptic-like activity prevailed (fig. S2). The same trend was also observed in the computational model of spiking neurons (fig. S8). The fundamental role of inhibition in shaping asynchronous states has been explored both experimentally and theoretically, revealing that networks of purely excitatory neurons are not able to generate stable asynchronous states (*17*). The critical role of inhibition in stabilizing system dynamics (*50*) and in increasing input-dependent flexibility (figs. S2 and S8) highlights the evolutionary significance of preserving the balance of electrical-chemical signal transduction in the nervous system.

It has been conjectured that the function of neural networks requires the segregated processing of diverse inputs in specialized circuits as well as the integration of all of them to generate high-level information processing and response (*73*). This demands a flexible balance of segregation and integration, the loss of which may induce dysfunction (*74*). In dynamical terms, such an optimal balance is necessarily associated with high diversity and variability of underlying synchronization patterns of neuronal activity to be sustained (*75*). Therefore, understanding how network structural features and dynamical aspects collectively shape complex synchronization patterns is crucial for advances in the field. Our findings might also be relevant to understand other networked systems that have modular architectures and are subjected to noise, such as gene, epidemic, and social networks.

MATERIALS AND METHODS
Micropatterned substrate
Microcontact printing was used to pattern protein ink onto glass coverslips. First, glass coverslips (C018001, Matsunami Glass Ind.) were cleaned by sonication in 100% ethanol, rinsed in Milli-Q water, and treated with air plasma for 60 s (PM-100, Yamato). The cleaned coverslips were then treated with a 0.2% solution of poly(2-

methacryloyloxyethyl phosphorylcholine-co-3-methacryloxypropyl triethoxysilane) (*76*) in ethanol for 10 s, dried in an ethanol environment for 20 min, baked in an oven at 70°C for 4 hours, and dried under vacuum overnight. The coverslips were then sterilized by immersion in ethanol, rinsed in Milli-Q water, and dried. Protein ink [extracellular matrix gel (E1270, Sigma-Aldrich; 1:100 dilution) + poly-D-lysine (50 μg ml^{-1}; P0899, Sigma-Aldrich)] was patterned using a polydimethylsiloxane (PDMS) stamp. The fabrication of the PDMS stamp has been detailed previously (*44*). Four pieces of thin PDMS films (approximately 2 mm by 2 mm and 0.5-mm thickness) were then attached to the periphery of the coverslip, which served as spacers. Last, the coverslips were dried overnight in a fume hood and immersed in neuronal plating medium [minimum essential medium (MEM; 11095-080, Gibco) + 5% fetal bovine serum +0.6% D-glucose].

Cell culture
The culture protocol of primary rat cortical neurons has been described previously (*44*, *77*). Briefly, primary neurons were obtained from the cortices of embryonic day 18 pups, plated on a microfabricated coverslip at a density of 360 to 480 cells mm^{-2}, and cocultured with astrocyte feeder cells in N2 medium containing MEM + N2 supplement + ovalbumin (0.5 mg ml^{-1}) + 10 mM Hepes. Half of the medium was changed at day in vitro (DIV) 4 and DIV 8 with a conditioned neurobasal medium containing neurobasal (21103-049, Gibco) + 2% B-27 supplement (17504-044, Gibco) + 1% GlutaMAX-I (35050-061, Gibco). In some experiments, neurons were cultured in the neuron culture medium (FujiFilm Wako Pure Chemical Corp. 148-09671), a glia-conditioned medium. The astrocyte feeder layer was not used when culturing the neurons in the latter medium.

During cultivation, neurons were transfected with adeno-associated virus (AAV) vectors encoding the fluorescent calcium probe GCaMP6s (Addgene viral prep #100843-AAV9) and a red-shifted channelrhodopsin ChrimsonR (Addgene viral prep #59171-AAV9) under the Synapsin promotor. The as-received viral preparations were aliquoted and added at concentrations of 1 μl ml^{-1} (GCaMP6s) and 0.7 μl ml^{-1} (ChrimsonR) at DIV 4. The AAVs were diluted during medium exchange but remained in the growth medium until the end of the culture. All procedures were approved by the Tohoku University Center for Laboratory Animal Research, Tohoku University (approval number: 2020AmA-001) and Tohoku University Center for Gene Research (2019AmLMO-001).

Calcium imaging
At DIV 10 to 11, the coverslips with micropatterned neurons were rinsed in Hepes-buffered saline (HBS) containing 128 mM NaCl, 4 mM KCl, 1 mM CaCl$_2$, 1 mM MgCl$_2$, 10 mM D-glucose, 10 mM Hepes, and 45 mM sucrose and transferred to a glass-bottom dish (3960-035, Iwaki) filled with HBS (*44*, *77*). GCaMP6s fluorescence was imaged using an inverted microscope (Olympus IX83) equipped with a 20× objective lens (numerical aperture, 0.75), a white-light light-emitting diode (LED) (Sutter Lambda HPX), a scientific complementary metal-oxide-semiconductor camera (Andor Zyla 4.2P), and a stage-top incubator (Tokai Hit). All recordings were performed at 37°C, inside the stage-top incubator that kept the temperature constant and humidified the sample. All recordings were performed approximately 10 min after transferring the sample

from the cell culture incubator to the stage-top incubator, to eliminate the potential effect of environmental temperature on neuronal activity (*78*). Two networks were selected from a coverslip for the recording. A recording session of a network consisted of three phases: Phase 1 was a spontaneous activity recording, phase 2 a recording with optogenetic stimulation (see below), and phase 3 a spontaneous activity recording. Each phase lasted for 10 min, and time-lapse images were taken at 20 frames s^{-1} using Solis software (Andor).

Stimulation
For the optogenetic stimulation, patterned light illumination for activating ChrimsonR was delivered using a digital micromirror device (DMD) (Mightex Polygon400G) coupled to a high-power LED (Thorlabs Solis 623C; nominal wavelength, 623 nm) via a liquid light guide. The DMD was mounted on the inverted microscope, and patterned light was reflected onto the sample stage using a short-pass dichroic mirror with an edge frequency of 556 nm (Semrock FF556-SDi01). The spatiotemporal pattern of light illumination was designed in custom MATLAB script and programmed to the DMD using PolyScan2 software (Mightex). In the MATLAB script, somas of 10 neurons expressing ChrimsonR were randomly selected from the lower half of the cultured neuronal network. Subsequently, a circular illumination area centered around the soma (diameter, 25 μm) was generated randomly with a probability of 40% for each position. Last, 750 black-and-white bitmap files with the illumination pattern were generated and imported into PolyScan2. The duration of each frame was set to 400 ms, which was sufficiently long to initiate one or more spiking activities in the illuminated neuron. Identical spatiotemporal patterns were repeated in the first and second halves of the 10-min session. Chemical stimulation was realized by increasing the extracellular potassium concentration from 4 to 6 mM.

Spike detection
To extract the neuronal activity, regions of interest (ROIs) were manually set around the neuronal somas using the CellMagicWand plugin in ImageJ2, and the mean intensity within the ROIs was extracted for each time step. ROIs with no activity were not used, and an equal number of neurons were selected from each of the four modules. Spikes were detected from calcium fluorescence traces using the MLSpike algorithm (*79*). The first 1 min of each 10-min recording was removed to eliminate artifacts originating from the session onset. The algorithm occasionally detected pulse signals originating in the residual stimulation light as spikes, which were manually inspected and removed based on their shape and duration.

SNN model
The neurons were modeled using as LIF neurons, as described previously (*18*, *80*). In short, the single-neuron dynamics are described by the coupled differential equations

$$\tau_v \dot{v} = a(v - v_{ref})(v - v_{thr}) - u + I_{AMPA} - I_{GABA}$$
$$\tau_u \dot{u} = b(v - v_{ref}) - u$$

where v and u are variables representing the membrane potential and membrane recovery, respectively (with time constants τ_x). Neurons interact through excitatory and inhibitory currents

(I_{AMPA} and I_{GABA}), which are described by a relaxation $\tau_x \dot{I}_x = -I_x$ and are increased instantaneously at the postsynaptic neuron upon presynaptic firing by $I_{x,post} \rightarrow I_{x,post} + j_{x,pre} R_{pre}$, where $j_{x,pre}$ is a constant to describe the current strength, and R is the presynaptic resource variable that decreases upon firing by $R \rightarrow \beta R$ and recovers as $\tau_R \dot{R} = 1 - R$. In addition, all neurons are spontaneously driven by a Poisson shot noise added to I_{AMPA}, which accounts for spontaneous synaptic release and, depending on the noise rate, the optogenetic stimulation.

A modular network was constructed by considering four squares (200 μm by 200 μm) separated by 200 μm, locating 40 neurons randomly within each square, and simulating axon growth. Of these, 80% were excitatory neurons and 20% were inhibitory neurons, resembling the ratio reported for both in vivo and in vitro networks of the mammalian cortex (*49*, *81*, *82*). To create a model with k intermodular connections, the corresponding number of axons was forced to grow between each pair of modules. Binary adjacency matrices were then generated by forming synaptic connections when the axon of a presynaptic neuron intersected a circular region around a postsynaptic neuron within a radius of 150 ± 20 μm (mean ± SD). The corresponding connection probability was adjusted for each topology, so that the average in-degree per neuron was fixed to $k_{in} \sim 30$. Full details of the model are provided in section S2 (figs. S4 to S9).

Mesoscopic model

Each node i in the mesoscopic model corresponds to a module, and its dynamics were modeled using a coupled rate model with resource depletion (*12*)

$$\dot{\rho}_i(t) = -\frac{1}{\tau_\rho}\rho_i(t) + F[I_i(t)] + \sigma\xi_i(t)$$

$$\dot{R}_i(t) = -\frac{1}{\tau_d}\rho_i(t)R_i(t) + \frac{1}{\tau_c}[R_0 - R_i(t)]$$

where ρ and R are firing rate and synaptic resource variables, respectively, R_0 is the baseline resource level, and τ_x are time constants. $F(I_i)$ is a nonlinear function mapping the total input to module i, I_i, to a rate change (section S3A). Modules were spontaneously driven by Gaussian noise ξ with an amplitude σ, which was associated with internal biological variability.

Network models were constructed by coupling four modules together in a grid-like pattern (as in the 1-b and 3-b topologies), encoded by the adjacency matrix $A = [A_{ij}]$. Then, I_i was the sum of external input h, activity propagation within the module, and activity propagation from connected neighbors

$$I_i(t) = h + \rho_i(t)R_i(t) + w\sum_{j \neq i} A_{ij}g_{ij}(t)\rho_j(t)R_j(t)$$

where w is the coupling strength, and g_{ij} is the gating variable that describes whether modules i-j are connected or disconnected. h was varied to simulate perturbed conditions. The merged topology in the experiments corresponded to the behavior of a single module unit. Further details of the model are provided in section S3 (figs. S10 to S12).

Data analysis

For the analysis of collective activity events in the experimental data, the spike trains were first summed across all neurons and convolved with a normalized Gaussian kernel (SD = 200 ms), yielding a continuous time series that resembles a network-wide firing rate (averaged either per module or the whole population). The start and end times of the events were then obtained by thresholding the population rate at 10% of the maximum observed for any recording. An event thus begins whenever the population rate exceeds the threshold and ends when the rate drops below the threshold. To account for fluctuations during an event, we also merged consecutive events if a start time was separated by less than 100 ms from a previous end time. Event size was then defined as the number of unique neurons that contributed to the event normalized by the total number of neurons in the network. Events in SNN models were defined analogously to experiments with the following parameters: SD of the Gaussian kernel = 20 ms and threshold = 2.5%. The adjustments were motivated by designing a kernel that scaled with the shortest observed interspike interval and were necessary to account for the different sampling rates in simulations (5 ms) and experiments (50 ms).

To measure neuron correlation, Pearson correlation coefficients r_{ij} were calculated to quantify the synchronicity between a given pair of neurons i-j. For this analysis, the spike train was binned at 500 ms, and the number of spikes in each time bin was counted for each neuron. From here, r_{ij} was calculated by

$$r_{ij} = \frac{\sum_t [x_i(t) - \overline{x}_i][x_j(t) - \overline{x}_j]}{\sqrt{\sum_t [x_i(t) - \overline{x}_i]^2}\sqrt{\sum_t [x_j(t) - \overline{x}_j]^2}}$$

where $x_i(t)$ is the time-binned spike train of neuron i, and $\overline{x}_i$ is the time average of $x_i(t)$. When comparing to the mesoscopic model, we further calculated the module correlation as the Pearson correlation coefficient between the time series of module-averaged firing rates (calculated as described above).

The functional complexity χ (*48*) was evaluated as

$$\chi = 1 - \frac{m}{2(m-1)}\sum_{\mu=1}^{m}\left|p_\mu(r_{ij}) - \frac{1}{m}\right|$$

where $p_\mu(r_{ij})$ is the probability distribution of r_{ij} in bin μ, $m = 20$ is the number of bins for r_{ij} used to estimate the distribution, and $|.|$ denotes the absolute value. The definition of the error bars is described in the captions of the corresponding figures. Note that the choice of bin size (500 ms) affects the absolute value of correlation coefficients and functional complexity, and we confirmed that the reported results remain consistent with bin sizes of 250, 500, and 1000 ms.

Supplementary Materials

This PDF file includes:
Supplementary Text
Figs. S1 to S12
Tables S1 to S7
Legends for movies S1 to S8
References

Other Supplementary Material for this manuscript includes the following:
Movies S1 to S8

REFERENCES AND NOTES

1. W. R. Softky, C. Koch, The highly irregular firing of cortical cells is inconsistent with temporal integration of random EPSPs. *J. Neurosci.* **13**, 334–350 (1993).

2. A. Arieli, A. Sterkin, A. Grinvald, A. D. Aertsen, Dynamics of ongoing activity: Explanation of the large variability in evoked cortical responses. *Science* **273**, 1868–1871 (1996).

3. M. E. Raichle, The restless brain. *Brain Connect.* **1**, 3–12 (2011).

4. J. Aru, J. Aru, V. Priesemann, M. Wibral, L. Lana, G. Pipa, W. Singer, R. Vicente, Untangling cross-frequency coupling in neuroscience. *Curr. Opin. Neurobiol.* **31**, 51–61 (2015).

5. A. Fornito, A. Zalesky, E. Bullmore, in Fundamentals of brain network analysis. (Academic Press, 2016).

6. R. M. Hutchison, T. Womelsdorf, E. A. Allen, P. A. Bandettini, V. D. Calhoun, M. Corbetta, S. Penna, J. H. Duyn, G. H. Glover, J. Gonzalez-Castillo, D. A. Handwerker, S. Keilholz, V. Kiviniemi, D. A. Leopold, F. Pasquale, O. Sporns, M. Walter, C. Chang, Dynamic functional connectivity: Promise, issues, and interpretations. *Neuroimage* **80**, 360–378 (2013).

7. T. Matsui, T. Q. Pham, K. Jimura, J. Chikazoe, On co-activation pattern analysis and non-stationarity of resting brain activity. *Neuroimage* **249**, 118904 (2022).

8. J. M. Beggs, D. Plenz, Neuronal avalanches in neocortical circuits. *J. Neurosci.* **23**, 11167–11177 (2003).

9. R. Legenstein, W. Maass, Edge of chaos and prediction of computational performance for neural circuit models. *Neural Netw.* **20**, 323–334 (2007).

10. D. R. Chialvo, Emergent complex neural dynamics. *Nat. Phys.* **6**, 744–750 (2010).

11. L. Cocchi, L. L. Gollo, A. Zalesky, M. Breakspear, Criticality in the brain: A synthesis of neurobiology, models and cognition. *Prog. Neurobiol.* **158**, 132–152 (2017).

12. S. di Santo, P. Villegas, R. Burioni, M. A. Muñoz, Landau-Ginzburg theory of cortex dynamics: Scale-free avalanches emerge at the edge of synchronization. *Proc. Natl. Acad. Sci. U.S.A.* **115**, E1356 (2018).

13. M. A. Muñoz, *Colloquium*: Criticality and dynamical scaling in living systems. *Rev. Mod. Phys.* **90**, 031001 (2018).

14. B. Cramer, D. Stöckel, M. Kreft, M. Wibral, J. Schemmel, K. Meier, V. Priesemann, Control of criticality and computation in spiking neuromorphic networks with plasticity. *Nat. Commun.* **11**, 2853 (2020).

15. D. Plenz, T. L. Ribeiro, S. R. Miller, P. A. Kells, A. Vakili, Self-organized criticality in the brain. *Front. Phys.* **9**, 639389 (2021).

16. N. Brunel, Dynamics of sparsely connected networks of excitatory and inhibitory spiking neurons. *J. Comput. Neurosci.* **8**, 183–208 (2000).

17. A. Renart, J. de la Rocha, P. Bartho, L. Hollender, N. Parga, A. Reyes, K. D. Harris, The asynchronous state in cortical circuits. *Science* **327**, 587–590 (2010).

18. J. G. Orlandi, J. Soriano, E. Alvarez-Lacalle, S. Teller, J. Casademunt, Noise focusing and the emergence of coherent activity in neuronal cultures. *Nat. Phys.* **9**, 582–590 (2013).

19. P. Fries, Rhythms for cognition: Communication through coherence. *Neuron* **88**, 220–235 (2015).

20. P. Villegas, P. Moretti, M. A. Muñoz, Frustrated hierarchical synchronization and emergent complexity in the human connectome network. *Sci. Rep.* **4**, 5990 (2014).

21. M. I. Rabinovich, P. Varona, A. Selverston, H. D. I. Abarbanel, Dynamical principles in neuroscience. *Rev. Mod. Phys.* **78**, 1213–1265 (2006).

22. E. Tognoli, J. A. S. Kelso, The metastable brain. *Neuron* **81**, 35–48 (2014).

23. O. Weinberger, P. Ashwin, From coupled networks of systems to networks of states in phase space. *Discrete Continuous Dyn. Syst. Ser. B* **23**, 2043–2063 (2018).

24. L. Donetti, P. I. Hurtado, M. A. Muñoz, Entangled networks, synchronization, and optimal network topology. *Phys. Rev. Lett.* **95**, 188701 (2005).

25. A. Arenas, A. Diaz-Guilera, J. Kurths, Y. Moreno, C. Zhou, Synchronization in complex networks. *Phys. Rep.* **469**, 93–153 (2008).

26. Y. M. Lai, M. A. Porter, Noise-induced synchronization, desynchronization, and clustering in globally coupled nonidentical oscillators. *Phys. Rev. E* **88**, 012905 (2013).

27. M. Dazza, S. Métens, P. Monceau, S. Bottani, A novel methodology to describe neuronal networks activity reveals spatiotemporal recruitment dynamics of synchronous bursting states. *J. Comput. Neurosci.* **49**, 375–394 (2021).

28. A. Y. Y. Tan, Y. Chen, B. Scholl, E. Seidemann, N. J. Priebe, Sensory stimulation shifts visual cortex from synchronous to asynchronous states. *Nature* **509**, 226–229 (2014).

29. J. Zierenberg, J. Wilting, V. Priesemann, Homeostatic plasticity and external input shape neural network dynamics. *Phys. Rev. X* **8**, 031018 (2018).

30. R. M. Bruno, B. Sakmann, Cortex is driven by weak but synchronously active thalamo-cortical synapses. *Science* **312**, 1622–1627 (2006).

31. K. C.-K. Malina, B. Mohar, A. N. Rappaport, I. Lampl, Local and thalamic origins of correlated ongoing and sensory-evoked cortical activities. *Nat. Commun.* **7**, 12740 (2016).

32. H. Mizuno, K. Ikezoe, S. Nakazawa, T. Sato, K. Kitamura, T. Iwasato, Patchwork-type spontaneous activity in neonatal barrel cortex layer 4 transmitted via thalamocortical projections. *Cell Rep.* **22**, 123–135 (2018).

33. M. H. Friedberg, S. M. Lee, F. F. Ebner, Modulation of receptive field properties of thalamic somatosensory neurons by the depth of anesthesia. *J. Neurophysiol.* **81**, 2243–2252 (1999).

34. D. S. Greenberg, A. R. Houweling, J. D. Kerr, Population imaging of ongoing neuronal activity in the visual cortex of awake rats. *Nat. Neurosci.* **11**, 749–751 (2008).

35. W.-P. Chang, J.-S. Wu, C.-M. Lee, B. A. Vogt, B.-C. Shyu, Spatiotemporal organization and thalamic modulation of seizures in the mouse medial thalamic-anterior cingulate slice. *Epilepsia* **52**, 2344–2355 (2011).

36. Ł. Kuśmierz, S. Ogawa, T. Toyoizumi, Edge of chaos and avalanches in neural networks with heavy-tailed synaptic weight distribution. *Phys. Rev. Lett.* **125**, 028101 (2020).

37. C. W. Lynn, D. S. Bassett, The physics of brain network structure, function and control. *Nat. Rev. Phys.* **1**, 318–332 (2019).

38. J. W. Scannell, M. P. Young, The connectional organization of neural systems in the cat cerebral cortex. *Curr. Biol.* **3**, 191–200 (1993).

39. J. W. Scannell, G. A. P. C. Burns, C. C. Hilgetag, M. A. O'Neil, M. P. Young, The connectional organization of the cortico-thalamic system of the cat. *Cereb. Cortex* **9**, 277–299 (1999).

40. C.-C. Hilgetag, G. A. P. C. Burns, M. A. O'Neill, J. W. Scannell, M. P. Young, Anatomical connectivity defines the organization of clusters of cortical areas in the macaque monkey and the cat. *Phil. Trans. R. Soc. Lond. B* **355**, 91–110 (2000).

41. D. Meunier, R. Lambiotte, E. T. Bullmore, Modular and hierarchically modular organization of brain networks. *Front. Neurosci.* **4**, 200 (2010).

42. M. P. van den Heuvel, E. T. Bullmore, O. Sporns, Comparative connectomics. *Trends Cogn. Sci.* **20**, 345–361 (2016).

43. W.-C. A. Lee, V. Bonin, M. Reed, B. J. Graham, G. Hood, K. Glattfelder, R. C. Reid, Anatomy and function of an excitatory network in the visual cortex. *Nature* **532**, 370–374 (2016).

44. H. Yamamoto, S. Moriya, K. Ide, T. Hayakawa, H. Akima, S. Sato, S. Kubota, T. Tanii, M. Niwano, S. Teller, J. Soriano, A. Hirano-Iwata, Impact of modular organization on dynamical richness in cortical networks. *Sci. Adv.* **4**, eaau4914 (2018).

45. J. L. Nathanson, Y. Yanagawa, K. Obata, E. M. Callaway, Preferential labeling of inhibitory and excitatory cortical neurons by endogenous tropism of adeno-associated virus and lentivirus vectors. *Neuroscience* **161**, 441–450 (2009).

46. N. C. Klapoetke, Y. Murata, S. S. Kim, S. R. Pulver, A. Birdsey-Benson, Y. K. Cho, T. K. Morimoto, A. S. Chuong, E. J. Carpenter, Z. J. Tian, J. Wang, Y. L. Xie, Z. X. Yan, Y. Zhang, B. Y. Chow, B. Surek, M. Melkonian, V. Jayaraman, M. Constantine-Paton, G. K. S. Wong, E. S. Boyden, Independent optical excitation of distinct neural populations. *Nat. Methods* **11**, 338–346 (2014).

47. Y. Penn, M. Segal, E. Moses, Network synchronization in hippocampal neurons. *Proc. Natl. Acad. Sci. U.S.A.* **113**, 3341–3346 (2016).

48. G. Zamora-López, Y. Chen, G. Deco, M. L. Kringelbach, C. Zhou, Functional complexity emerging from anatomical constraints in the brain: The significance of network modularity and rich-clubs. *Sci. Rep.* **6**, 38424 (2016).

49. N. Sukenik, O. Vinogradov, E. Weinreb, M. Segal, A. Levina, E. Moses, Neuronal circuits overcome imbalance in excitation and inhibition by adjusting connection numbers. *Proc. Natl. Acad. Sci. U.S.A.* **118**, e2018459118 (2021).

50. S. Sadeh, C. Clopath, Inhibitory stabilization and cortical computation. *Nat. Rev. Neurosci.* **22**, 21–37 (2021).

51. D. Cohen, M. Segal, Network bursts in hippocampal microcultures are terminated by exhaustion of vesicle pools. *J. Neurophysiol.* **106**, 2314–2321 (2011).

52. E. Tibau, M. Valencia, J. Soriano, Identification of neuronal network properties from the spectral analysis of calcium imaging signals in neuronal cultures. *Front. Neural Circuits* **7**, 199 (2013).

53. E. A. Leicht, M. E. J. Newman, Community structure in directed networks. *Phys. Rev. Lett.* **100**, 118703 (2008).

54. S. Teller, C. Granell, M. De Domenico, J. Soriano, S. Gómez, A. Arenas, Emergence of assortative mixing between clusters of cultured neurons. *PLOS Comput. Biol.* **10**, e1003796 (2014).

55. M. A. Rabadan, E. D. De La Cruz, S. B. Rao, Y. Chen, C. Gong, G. Crabtree, B. Zu, S. Markx, J. A. Gogos, R. Yuste, R. Tomer, An in vitro model of neuronal ensembles. *Nat. Commun.* **13**, 3340 (2022).

56. B. Pietras, V. Schmutz, T. Schwalger, Mesoscopic description of hippocampal replay and metastability in spiking neural networks with short-term plasticity. *PLOS Comput. Biol.* **18**, e1010809 (2022).

57. J. P. Neto, F. P. Spitzner, V. Priesemann, Sampling effects and measurement overlap can bias the inference of neuronal avalanches. *PLOS Comput. Biol.* **18**, e1010678 (2022).

58. E. Montbrió, D. Pazó, A. Roxin, Macroscopic description for networks of spiking neurons. *Phys. Rev. X* **5**, 021028 (2015).

59. Á. Byrne, R. D. O'Dea, M. Forrester, J. Ross, S. Coombes, Next-generation neural mass and field modeling. *J. Neurophysiol.* **123**, 726–742 (2020).

60. C. Bick, M. Goodfellow, C. R. Laing, E. A. Martens, Understanding the dynamics of biological and neural oscillator networks through exact mean-field reductions: A review. *J. Math. Neurosci.* **10**, 9 (2020).

61. I. V. Tyulkina, D. S. Goldobin, L. S. Klimenko, A. Pikovsky, Dynamics of noisy oscillator populations beyond the Ott-Antonsen ansatz. *Phys. Rev. Lett.* **120**, 264101 (2018).

62. S. M. Sherman, R. W. Guillery, The role of the thalamus in the flow of information to the cortex. *Phil. Trans. R. Soc. Lond. B* **357**, 1695–1708 (2002).

63. M. D. McDonnell, L. M. Ward, The benefits of noise in neural systems: Bridging theory and experiment. *Nat. Rev. Neurosci.* **12**, 415–425 (2011).

64. G. Shahaf, S. Marom, Learning in networks of cortical neurons. *J. Neurosci.* **21**, 8782–8788 (2001).

65. D. A. Wagenaar, R. Madhavan, J. Pine, S. M. Potter, Controlling bursting in cortical cultures with closed-loop multi-electrode stimulation. *J. Neurosci.* **25**, 680–688 (2005).

66. M. Chiappalone, P. Massobrio, S. Martinoia, Network plasticity in cortical assemblies. *Eur. J. Neurosci.* **28**, 221–237 (2008).

67. X. Zhang, F.-C. Yeh, H. Ju, Y. Jiang, G. F. W. Quan, A. M. J. VanDongen, Familiarity detection and memory consolidation in cortical assemblies. *eNeuro* **7**, ENEURO.0006–19.2020 (2020).

68. Y. Inglebert, J. Aljadeff, N. Brunel, D. Debanne, Synaptic plasticity rules with physiological calcium levels. *Proc. Natl. Acad. Sci. U.S.A.* **117**, 33639–33648 (2020).

69. S. Okujeni, U. Egert, Self-organization of modular network architecture by activity-dependent neuronal migration and outgrowth. *eLife* **8**, e47996 (2019).

70. S. Okujeni, U. Egert, Structural modularity tunes mesoscale criticality in biological neuronal networks. *J. Neurosci.* **43**, 2515–2526 (2023).

71. F. M. Krienen, M. Goldman, Q. Zhang, R. C. H. del Rosario, M. Florio, R. Machold, A. Saunders, K. Levandowski, H. Zaniewski, B. Schuman, C. Wu, A. Lutservitz, C. D. Mullally, N. Reed, E. Bien, L. Bortolin, M. Fernandez-Otero, J. D. Lin, A. Wysoker, J. Nemesh, D. Kulp, M. Burns, V. Tkachev, R. Smith, C. A. Walsh, J. Dimidschstein, B. Rudy, L. S. Kean, S. Berretta, G. Fishell, G. Feng, S. A. McCarroll, Innovations present in the primate interneuron repertoire. *Nature* **586**, 262–269 (2020).

72. S. Loomba, J. Straehle, V. Gangadharan, N. Heike, A. Khalifa, A. Motta, N. Ju, M. Sievers, J. Gempt, H. S. Meyer, M. Helmstaedter, Connectomic comparison of mouse and human cortex. *Science* **377**, eabo0924 (2022).

73. G. Tononi, O. Sporns, G. M. Edelman, A measure for brain complexity: Relating functional segregation and integration in the nervous system. *Proc. Natl. Acad. Sci. U.S.A.* **91**, 5033–5037 (1994).

74. L.-D. Lord, A. B. Stevner, G. Deco, M. L. Kringelbach, Understanding principles of integration and segregation using whole-brain computational connectomics: Implications for neuropsychiatric disorders. *Philos. Trans. A Math. Phys. Eng. Sci.* **375**, 20160283 (2017).

75. G. Deco, V. K. Jirsa, P. A. Robinson, M. Breakspear, K. Friston, The dynamic brain: From spiking neurons to neural masses and cortical fields. *PLOS Comput. Biol.* **4**, e1000092 (2008).

76. Y. Xu, M. Takai, T. Konno, K. Ishihara, Microfluidic flow control on charged phospholipid-polymer interface. *Lab Chip* **7**, 199–206 (2007).

77. H. Yamamoto, S. Kubota, Y. Chida, M. Morita, S. Moriya, H. Akima, S. Sato, A. Hirano-Iwata, T. Tanii, M. Niwano, Size-dependent regulation of synchronized activity in living neuronal networks. *Phys. Rev. E* **94**, 012407 (2016).

78. C. M. Hales, J. D. Rolston, S. M. Potter, How to culture, record and stimulate neuronal networks on micro-electrode arrays (MEAs). *J. Vis. Exp.* **39**, 2056 (2010).

79. T. Deneux, A. Kaszas, G. Szalay, G. Katona, T. Lakner, A. Grinvald, B. Rózsa, I. Vanzetta, Accurate spike estimation from noisy calcium signals for ultrafast three-dimensional imaging of large neuronal populations in vivo. *Nat. Commun.* **7**, 12190 (2016).

80. E. M. Izhikevich, Simple model of spiking neurons. *IEEE Trans. Neural Netw.* **14**, 1569–1572 (2003).

81. S. Sahara, Y. Yanagawa, D. D. M. O'Leary, C. F. Stevens, The fraction of cortical GABAergic neurons is constant from near the start of cortical neurogenesis to adulthood. *J. Neurosci.* **32**, 4755–4761 (2012).

82. J. Soriano, M. R. Martínez, T. Tlusty, E. Moses, Development of input connections in neural cultures. *Proc. Natl. Acad. Sci. U.S.A.* **105**, 13758–13763 (2008).

83. T. Takemuro, H. Yamamoto, S. Sato, A. Hirano-Iwata, Polydimethylsiloxane microfluidic films for in vitro engineering of small-scale neuronal networks. *Jpn. J. Appl. Phys.* **59**, 117001 (2020).

84. M. Newman, in *Networks* (Oxford University Press, ed. 2, 2018).

85. R. Guimerà, M. Sales-Pardo, L. A. Nunes Amaral, Modularity from fluctuations in random graphs and complex networks. *Phys. Rev. E* **70**, 025101(R) (2004).

86. E. Alvarez-Lacalle, E. Moses, Slow and fast pulses in 1-D cultures of excitatory neurons. *J. Comput. Neurosci.* **26**, 475–493 (2009).

87. J. S. Isaacson, M. Scanziani, How inhibition shapes cortical activity. *Neuron* **72**, 231–243 (2011).

88. K. A. Ferguson, F. Njap, W. Nicola, F. K. Skinner, S. A. Campbell, Examining the limits of cellular adaptation bursting mechanisms in biologically-based excitatory networks of the hippocampus. *J. Comput. Neurosci.* **39**, 289–309 (2015).

89. M. Stimberg, R. Brette, D. F. Goodman, Brian 2, an intuitive and efficient neural simulator. *eLife* **8**, e47314 (2019).

90. L. Huang, P. Ledochowitsch, U. Knoblich, J. Lecoq, G. J. Murphy, R. C. Reid, S. E. J. de Vries, C. Koch, H. Zeng, M. A. Buice, J. Waters, L. Li, Relationship between simultaneously recorded spiking activity and fluorescence signal in GCaMP6 transgenic mice. *eLife* **10**, e51675 (2021).

91. H. R. Wilson, J. D. Cowan, Excitatory and inhibitory interactions in localized populations of model neurons. *Biophys. J.* **12**, 1–24 (1972).

92. M. Jedynak, Collective excitability in a mesoscopic neuronal model of epileptic activity. *Phys. Rev. E* **97**, 012204 (2018).

93. W. Gerstner, W. M. Kistler, R. Naud, L. Paninski, in *Neuronal dynamics: From single neurons to networks and models of cognition* (Cambridge Univ. Press, 2014).

94. M. V. Tsodyks, H. Markram, The neural code between neocortical pyramidal neurons depends on neurotransmitter release probability. *Proc. Natl. Acad. Sci. U.S.A.* **94**, 719–723 (1997).

95. D. Holcman, M. Tsodyks, The emergence of Up and Down states in cortical networks. *PLOS Comput. Biol.* **2**, e23 (2006).

96. V. Buendía, P. Villegas, R. Burioni, M. A. Muñoz, Hybrid-type synchronization transitions: Where incipient oscillations, scale-free avalanches, and bistability live together. *Phys. Rev. Research* **3**, 023224 (2021).

97. P. C. Bressloff, J. N. Maclaurin, Stochastic hybrid systems in cellular neuroscience. *J. Math. Neurosci.* **8**, 12 (2018).

Science Advances

Modular architecture facilitates noise-driven control of synchrony in neuronal networks

Hideaki Yamamoto, F. Paul Spitzner, Taiki Takemuro, Victor Buenda, Hakuba Murota, Carla Morante, Tomohiro Konno, Shigeo Sato, Ayumi Hirano-Iwata, Anna Levina, Viola Priesemann, Miguel A. Muoz, Johannes Zierenberg, and Jordi Soriano

View the article online
https://www.science.org/doi/10.1126/sciadv.ade1755
Permissions
https://www.science.org/help/reprints-and-permissions

Use of this article is subject to the Terms of service